



## **Tools for Understanding Computational Behaviors of Bacterial Biofilms**

Jason Ho

Submitted in partial fulfillment of the requirements of the degree of  
Bachelor of Science with Honors in the School of Engineering at  
Brown University.

Prepared under the direction of:  
Professor Sherief Reda, Advisor  
Professor Jacob Rosenstein, Reader

---

Advisor's Signature

---

Reader's Signature

---

Honors Chair's Signature

April 15, 2022

# Contents

<b>1</b>	<b>Introduction</b>	<b>1</b>
1.1	Bacterial Biofilms . . . . .	3
1.2	Oscillator Based Computing . . . . .	4
<b>2</b>	<b>Related Work</b>	<b>7</b>
2.1	Other Oscillators in Computing Systems . . . . .	7
2.2	Super Resolution Techniques for EIT . . . . .	8
2.3	Models of Coupling Between Bacterial Biofilms . . . . .	9
<b>3</b>	<b>Impedance Image Processing Techniques</b>	<b>10</b>
3.1	Semiconductor Sensors . . . . .	10
3.2	Feature Matching between Image Mediums . . . . .	12
3.2.1	Traditional Feature Matching . . . . .	13
3.2.2	Clean Brightfield Microscope Image Matching . . . . .	15
3.3	Impedance Super-Resolution . . . . .	20
3.3.1	Imaging Unicellular Algae . . . . .	21
3.3.2	Shift-Sum Algorithm . . . . .	22
3.3.3	Linear Deconvolution Algorithm . . . . .	23
<b>4</b>	<b>Computational Modeling of Bacterial Biofilms</b>	<b>28</b>
4.1	Kuramoto Model . . . . .	29
4.2	Extrapolated N biofilm Biofilm Model . . . . .	30
4.3	Computer Microarchitectures of Biofilms . . . . .	33
4.3.1	Gate-Based Oscillator Computing . . . . .	33
<b>5</b>	<b>Conclusions and Future Work</b>	<b>35</b>
<b>6</b>	<b>Appendix</b>	<b>45</b>

# 1 Introduction

With the ever-growing complexity of computational algorithms and the omnipresence of computers, the environmental impact of silicon-based computing continues to grow at an unsustainable rate. For example, it is projected that information and communication technologies will account for 7% of global energy demand by 2030 [11]. Interestingly, 50-80% of the energy spent on chips comes from long wires and communication rather than computation [22], resulting in the proliferation of architectures where memory is close to computing centers. At the same time, Moore’s law, the doubling of transistors on chip every two years or so, is slowing due to heat and power delivery problems [30]. In addition to these problems, transistor channels are getting so small (tens of atoms) that quantum phenomena may dominate [30], compromising the original reliability of digital computing. While silicon hardware development is slowing down and reaching its fundamental limits, computer application complexity has no signs of slowing down, creating lots of research demand into technologies beyond silicon. Many of these systems are biologically inspired, such as spiking neural networks (SNNs), which mimic the human brain and perform similar tasks with great magnitudes of energy efficiency compared to traditional computing on the same task. If we are able to take advantage of the inherent efficiency of biological systems and manipulate them to perform meaningful computation, it could make way for ultra-low energy systems.

In this thesis, we focus on building an understanding of underlying mech-

anisms of bacterial biofilms and ways to manipulate them to perform useful computation. Bacterial biofilms are robust communities of bacteria that work together to survive unfavorable environments. We focus on them due to their widespread availability, enabling low-cost manufacturing at large scale, and their ability to communicate between one another [18]. Many mechanisms of biofilms are still unknown and difficult to continuously image under traditional microscope methods using fluorescence due to photo-toxicity and photo-bleaching [16] [28]. In addition, since these mechanisms are unknown, researchers do not know what to look for, which makes imaging difficult. Phototoxicity is the phenomenon in which excited fluorescence molecules produce reactive oxygen species that react with cell molecules such as proteins and lipids, causing cell death [12]. Similarly, photo-bleaching is caused by reactive oxygen species which react with other fluorescence molecules leading to a loss of signal in images [12]. These mechanisms make it difficult to take many complete microscope images in a short time span. Other imaging techniques, such as electrical impedance tomography (EIT), may be the solution, but they come with their own set of problems. EIT is a low-cost medical imaging technique that generates impedance mappings between electrode sensors, but suffers from low spatial resolution and thus robustness [5]. A main draw of EIT imaging is its ability to perform real-time imaging and monitoring of subjects [4] with the trade off of grey-scale imaging. While it is not possible to highlight certain processes using fluorescence in impedance imaging, recent work on generative adversarial networks (GANs) by Rivenson *et al.* suggests that fluorescence can be added using post processing deep-learning algorithms

[26]. Typically, GANs networks stay in the optical image domain, meaning that it is not clear whether it is possible to switch mediums from optical to impedance and achieve the same results. To begin to remedy these issues, we developed feature match detection algorithms between optical and impedance domains to generate robust data sets of bacterial biofilms that could be used to train such GANs deep learning models. In addition, we created a novel multi-impedance image super-resolution algorithm using linear deconvolution to improve spatial resolution of EIT images. Simultaneously, based on current knowledge of biofilm dynamics, we created a dynamical model to encompass the behavior of arrays of coupled biofilms and examined possible computational architectures.

## 1.1 Bacterial Biofilms

Biofilms are complex structures of single-celled organisms such as bacteria that have great resilience to environmental stress and adhere to a surface. Categorized as a “temporary multicellular lifestyle”, individual bacterium inside a biofilm communicate and work together to maximize nutrient utilization and survival [17]. Most of the biofilm is composed of extracellular matrix, which provides a shell of protection against the environment. In fact, this protection is a serious global health concern, allowing biofilms to withstand modern antibiotics, changes in pH, nutrient deprivation, and mechanical forces [27]. While this characteristic may be a major problem in medicine, it is a benefit to computing systems as its resilience enables the creation of long-time running systems able to withstand many different conditions.

Recent discoveries in bacterial biofilms have shown that they behave as electrochemical oscillators, establishing communication between the inner and exterior of the biofilm in order to share nutrients [18]. In addition, it has been shown that two separate biofilms that are spatially close together are coupled together and perform time-sharing of nutrients to maximize growth in nutrient-sparse conditions [18]. To optimize the use of nutrients, biofilms encode information about their environment and compute how to react for their collective benefit. This intelligence seems to contain computing power that we could harness. Along with communication, research has shown that bacterial biofilm membrane potentials can be encoded to create robust memory that persists through electrical signaling [33]. This behavior is particularly exciting as it is thought to be caused by changes in proteins, similar to memory in neurons [33].

## 1.2 Oscillator Based Computing

Since it has been demonstrated that bacterial biofilms oscillate and communicate between each other [18], it is possible to use them as the building blocks of complex coupled oscillator-based computing systems. Oscillator-based computing systems are not necessarily new, with oscillators such as spin torque oscillators and vanadium oxide oscillators, and are a wide area of research beyond traditional computing systems due to their ability to conserve energy [8].

In these systems, information is stored in the phase rather than the amplitude of signals and is biologically inspired by brains, which function and learn from oscillating signals [6]. Compared to traditional digital computers which work with boolean values, oscillating computers are able to encode a wide range of values which make them useful for applications that require analog-like values, such as image processing and neural networks.

Typically, oscillating computing systems are composed of arrays of coupled oscillators initialized to input values, such as image pixel amplitudes. Similar input phases will synchronize in-phase, while drastically different values will continue to oscillate out-of-phase. Once values converge, the computation is finished. One interesting property of coupled oscillators is the locality of memory in comparison to where the computation occurs. In traditional Von-Neumann computing models, the memory and centers for computation are separated from each other, creating a present-day memory interconnect bottleneck on silicon chips [22]. Another property of coupled oscillators is their inherent parallelization. Everything computes at the same time, meaning that oscillating computing systems perform exceptionally well in highly parallelizable processes such as convolution.

Bacterial biofilms are a new type of coupled oscillator that we will examine further because we believe that utilizing actual biological elements to compute rather than imitating biological processes will enable living, adaptable ultra-efficient computers. In addition, there is computation beyond the oscillating

nature of bacterial biofilms that we believe can be harnessed.

## 2 Related Work

In this section, we briefly cover work on oscillating computing building blocks, super-resolution techniques for EIT, and current models of bacterial biofilms.

### 2.1 Other Oscillators in Computing Systems

Oscillating computing architectures have been conceptualized with many different building blocks, such as spin torque oscillators [29], ring oscillators in silicon, laser-assisted spin torque oscillators [9], chemical reaction oscillators [24], and cardiac muscle oscillators [25]. Since these building blocks essentially use the same core architectures with slight modifications at different size scaling, we will focus on chemical and other biological oscillators in this section due to their similarity to biofilms, which may have communicate using chemical or electrical signals. In Parrilla-Gutierrez *et al.*, a  $5 \times 5$  array of chemical oscillators based on the Belousov–Zhabotinsky (BZ) chemical reaction was used to demonstrate an autoencoder [24]. The BZ reaction would oscillate between Fe(II) and Fe(III) generated by magnetic stir rods spinning in specific array cells. In Ren *et al.*, living heart cells were used as electrical oscillators and coupled with cardiac fibroblast cells to perform graph coloring, a traditionally difficult problem for computers to solve but easy for oscillating networks by nature of their synchronization behavior [25]. In both of these examples, their basic coupled oscillator arrays demonstrated the ability to compute the equivalent of millions of traditional operations per second [24] and solve some computationally difficult problems faster than boolean algorithms when scaled

larger. Their work suggests that we should find similar success in biofilm computing systems.

## 2.2 Super Resolution Techniques for EIT

The goal of super resolution techniques is to improve spatial resolution of images using many low-resolution images that contain subpixel differences between images. Typically, super-resolution techniques on optical images consist of stacking similar, shifted images together to create high resolution images that can capture sub-camera-sensor-pixel detail [7]. This is simply not possible on EIT images with irregularly arranged pixels as electrodes can be placed anywhere on the subject.

In electrical impedance tomography, we had previously stated that low spatial resolution is a large issue compared to other imaging techniques. In addition, errors in reconstruction algorithms and lack of sensitivity in some regions may be directly caused by electrode location precision when images are taken. Since algorithms cannot correct for an error in electrode location, EIT imaging is considered less robust. While it may not be possible to fix user electrode placement, there is research into super-resolution algorithms for EIT imaging to remedy low spatial resolution. Perhaps the most prominent paper by Borsoi *et al.* use aperiodic penrose tiling and resampling of EIT images to improve spatial resolution [4]. We note that in traditional EIT imaging, non-uniform electrode placement creates non-uniformly spaced pixels which is why

this super-resolution algorithm deviates from traditional methods where the position of pixels is constant.

### 2.3 Models of Coupling Between Bacterial Biofilms

While there are many papers that try to explain individual biofilm dynamics, Liu *et al.* introduce a simplified biofilm model that focuses primarily on capturing the coupled oscillation behavior between bacterial biofilms [18]. Their model was experimentally confirmed on two biofilms occupying the same microfluidic chamber and nutrient source and demonstrated synchronicity in nutrient-dense environments. Conversely, they demonstrated out-of-phase communication between separate bacterial biofilms under nutrient-sparse conditions. The mathematical model captures this behavior through nutrient consumption and replacement functions. This paper serves as the original framework for all further models discussed in this thesis. For further detail into the mathematical model, it is thoroughly described in Liu *et al.*'s paper in the supplementary material [18].

## 3 Impedance Image Processing Techniques

The following section first introduces the semiconductor EIT imaging sensor array that was utilized to collect data for all of the following experiments and the creation of algorithms. We then introduce the work performed on these CMOS sensor arrays including feature matching between optical and impedance images for robust data sets, and multi impedance image super-resolution algorithms to increase spatial resolution.

### 3.1 Semiconductor Sensors

The semiconductor sensor array utilized in developing all the image processing algorithms in question comes from Hu *et al.* and their  $512 \times 256$  pixel 180 nm CMOS biosensor array [15]. They use a switched capacitor circuit with non-overlapping clocks to measure impedance at a particular pixel and produces the raw EIT images [15]. Perhaps the largest difference between this sensor array and typical biomedical EIT imaging is the precision location of electrodes. The array is regular and is made using traditional silicon manufacturing, enabling precision placement and knowledge of electrode locations at each pixel. In addition to the original Electrical Impedance Spectroscopy (EIS) image at a single point, the array can capture the mutual capacitance between any two pixels, regardless of their distance as shown in **Figure 2** [14]. These additional images capture extra spatial information that may not be conferred in a single impedance image. This means that with many different low-spatial-resolution images of the same object with different offsets and slightly different informa-

tion, they can be combined to yield a higher-resolution image. In **Figure 1**, the sensor array is shown along with the PCB packaging and the Field Programmable Gate Array (FPGA).

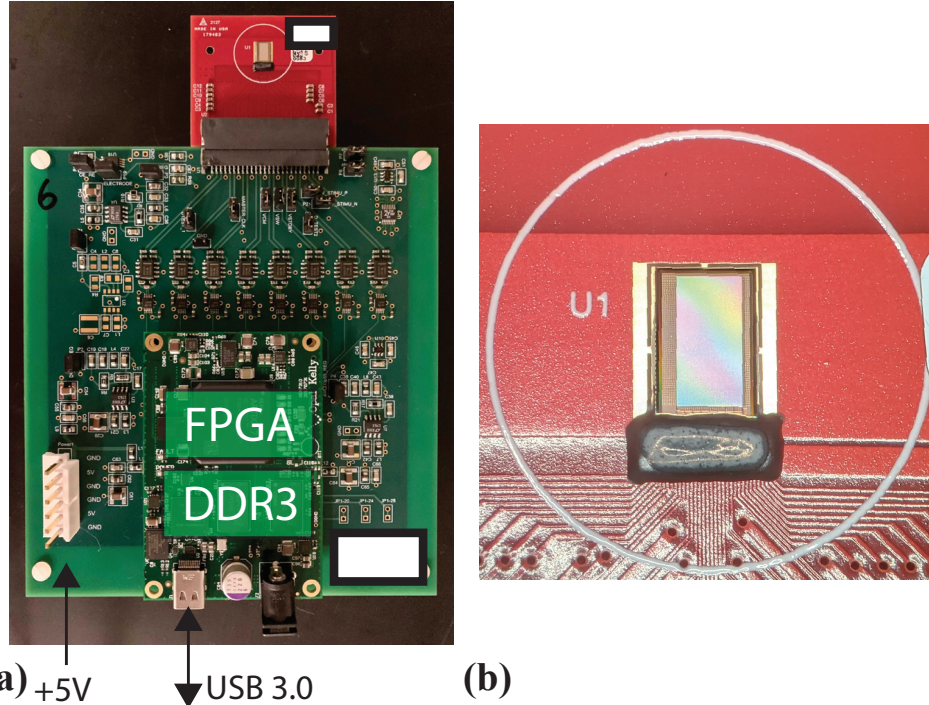


Figure 1: (a) Semiconductor 512 x 256 Impedance Sensor Array packaged on custom PCB with FPGA acquisition device. (b) Zoomed in image of sensor array on PCB package.

All experiments and impedance images in this thesis are taken from a semiconductor sensor similar to this system. Unlike microscopes that have lenses to magnify areas of interest, the objects are placed and grown right on top of the impedance array, meaning that image spatial resolution is highly dependent on pixel size. Although the technology node for the semiconductor can shrink as 180nm is an old technology, we focus on achieving sub-pixel resolution in

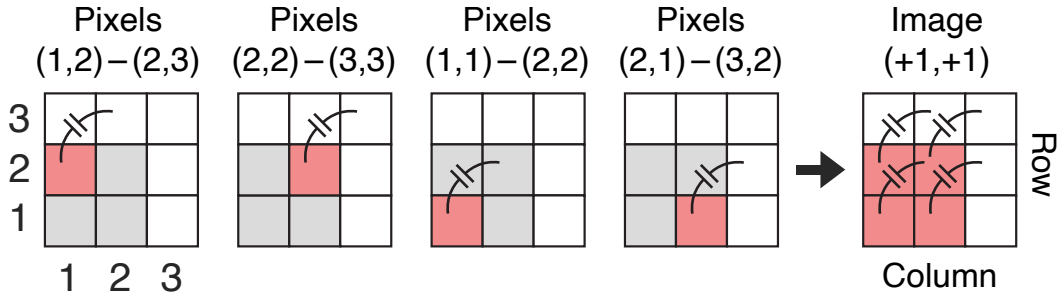


Figure 2: One EIS image is constructed from a collection of pairwise mutual capacitance measurements. Illustrated above is the construction of the image which measures  $C_M$  between each pixel and one of its diagonal neighbors, which we describe as a kernel offset of  $(\delta_i, \delta_j) = (+1, +1)$ . Different kernels can be used to produce different EIS images

the super-resolution section.

### 3.2 Feature Matching between Image Mediums

In order to develop future deep learning algorithms that can perform "virtual" staining of EIT images, it is necessary to create large robust data sets that spatially match the optical fluorescence images with the EIT images. Previously, this process was done by hand and was extremely tedious considering the skew, rotation, and differing resolutions of microscope and EIT images. An automated way to solve this problem is to perform feature matching between two different images and then match those points together so that the images are aligned using matrix transforms. In addition, deep learning models require large training sets, making hand-matching not very robust or practical.

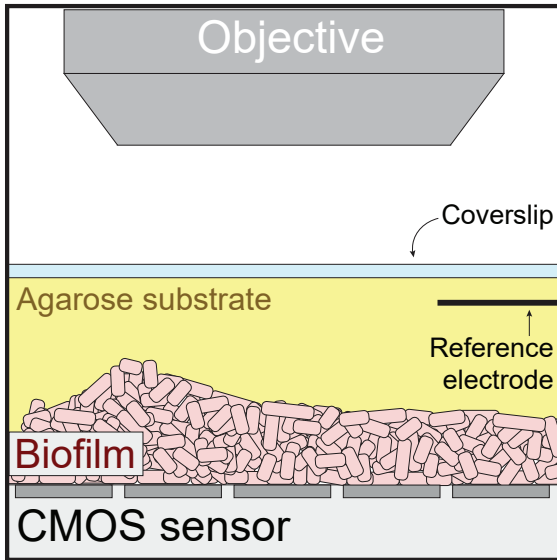


Figure 3: Illustration of experimental setup in which optical and CMOS impedance images are taken. The microscope will take images of the tops of biofilms while the impedance array will capture the footprint of biofilm structures. Figure reproduced from [15] with permission from the authors.

From **Figure 3**, we show the experimental setup used to take images of biofilms. Since one of the images is taken from the top (microscope), while the other is taken from the bottom (EIT), there will be inherent differences between the images which will make feature matching difficult. What is not included in the figure is the varying location, tilt, and scale variance associated with the microscope, enabling additional degrees of freedom that a feature matching algorithm will need to consider.

### 3.2.1 Traditional Feature Matching

Typically, feature matching between optical images is accomplished by finding feature points in each of the two respective images, describing each feature

point such that they can be represented uniquely, and then determining the closest match. This method provides us with pairs of different feature points which match to a certain degree of error between the two optical images.

Perhaps the most famous algorithm for detecting, describing features, and matching is Scale Invariant Feature Transform (SIFT) [19]. This involved algorithm finds feature points by searching for local extrema at different scale factors and then eliminating low-contrast rotation variant points. Each feature is described with a 128 length vector across a  $16 \times 16$  pixel area that includes information on the orientation and magnitude of the subset areas. The feature match is then accomplished by finding the smallest euclidean distance between descriptors in the 128 dimensional space, known as nearest neighbor matching. To ensure that the values make sense, a Lowe ratio test is performed to check that a feature match is not ambiguous by choosing matches where the second-best keypoint match is less than the best match by some ratio [19]. This algorithm is typically regarded as the standard for matching features and we utilize this algorithm in our own implementation for matching between image mediums.

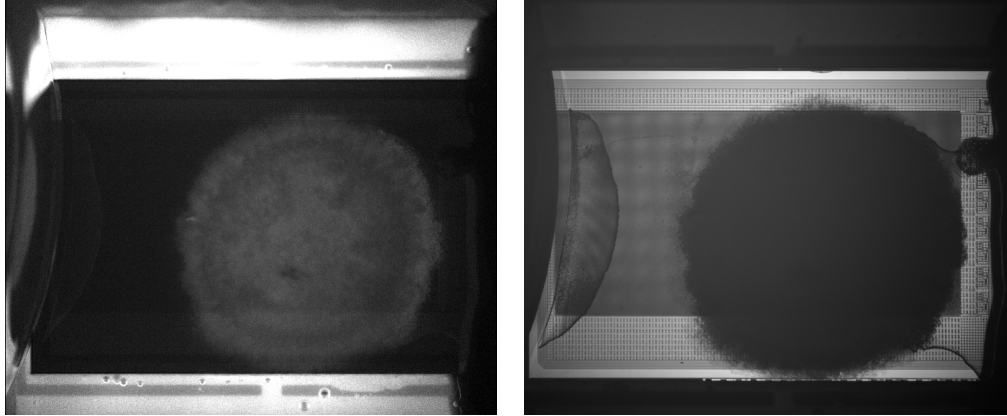
In our initial iteration of the feature match algorithm, we implement SIFT exactly as described in the previous section using OpenCV, which is an open source library containing common image processing tools [23], on an impedance image and its respective microscope image of a biofilm taken using a similar setup to **Figure 3**. The algorithm ran into countless problems and matched al-

most everything incorrectly, since matching feature points between the two different mediums would have very different keypoint descriptors. Each medium emphasized different features and each image was different due to the orientation of the sensor relative to the object.

### 3.2.2 Clean Brightfield Microscope Image Matching

To fix the problems highlighted in the previous section, we redefine the problem without using the impedance image by recognizing that the sensor array is rectangular. If we put a bounding box around the sensor array in the experimental optical image, match the semiconductor to a known image to identify the corners of the sensor and rectify the image onto the same plane as the impedance image using a matrix transform, we will get an optical image that looks and matches up with the impedance image. This method would eliminate the need to feature match between optical and impedance domains.

One other difference in approach was the use of brightfield images taken right before an experiment was conducted rather than experimental fluorescence. As shown in **Figure 4**, brightfield images provide more contrast between the object and the sensor chip, highlighting the sensor chip architecture, the sensor area, and surrounding logic rather than the subject. There would be more invariant image keypoints that a feature-match algorithm could match to on the sensor, which is highly standardized and should greatly improve accuracy. Using the brightfield image taken before the experiment assumes that the experimental setup moves negligibly during the length of the experiment. This



(a) mCherry fluorescence dye image of biofilm during experiment. (b) mCherry fluorescence dye brightfield image before experiment.

Figure 4: Microscope images of the same biofilm during the experiment showing fluorescence and before the experiment in brightfield.

should be a safe assumption because once the experiment is setup, it is typically not moved until the experiment finishes. The biofilm would still appear in the brightfield image as shown in **Figure 4b**, meaning that key feature points such as the sensor array corners could be blocked and feature match detection would still be necessary to establish robustness in our match. To make feature matching easier, we match against a brightfield image of a clean semiconductor chip with nothing growing on top. This maximizes our potential to find suitable matches, especially when the biofilm can grow to cover any part of the chip.

To illustrate the process of finding the sensor array, we go through an example to isolate and rectify the sensor array on an experimental brightfield image. After loading in a clean and experimental brightfield image, we can improve our accuracy in matching feature points by equalizing the contrast and bright-

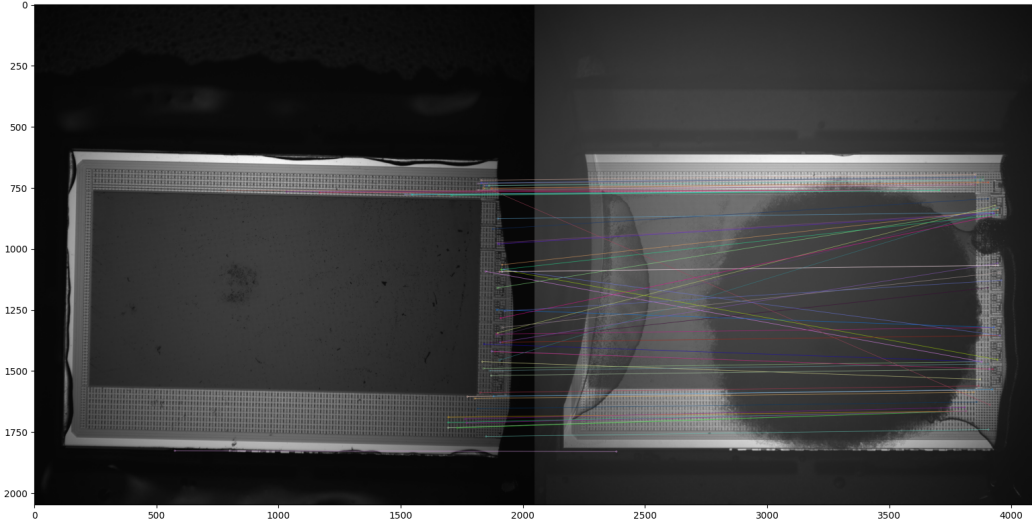


Figure 5: Initial SIFT feature matches between the clean brightfield image and the experimental brightfield image with ratio set to 0.6. The lines indicate a potential match.

ness histograms. We then perform SIFT and nearest neighbor matching with a Lowe ratio test, yielding an intermediate result that looks like **Figure 5**. In this figure, many of the lines correctly match between the two images, yet there are also some matches that do not make sense. If we want to estimate the matrix transform between the two images, we need to get only the matches that make sense. To do this, we use random sample consensus (RANSAC), an iterative outlier detection method that can robustly remove matches that are outliers, which typically gets rid of faulty matches [10].

With a subset of our original matches, we can finally estimate the homography or transform from one image plane to the other. This will give us the matrix to go from a point in one of the images to a point in the other. We previously determined by hand the coordinates of the corners of the sensor array on the

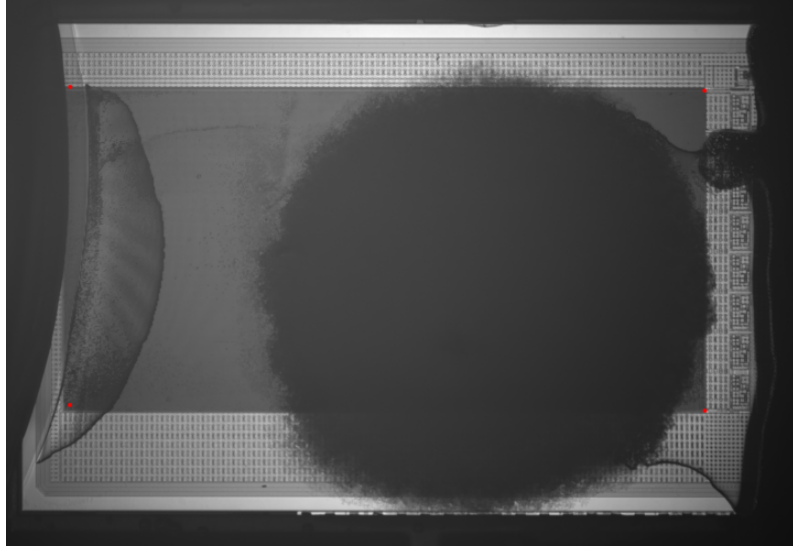


Figure 6: Experimental brightfield image with estimated corners highlighted in red from estimation of matrix transform from known corners on clean bright-field image.

clean brightfield image, meaning that the homography matrix will estimate the corners on the experimental image. Since the clean chip image does not change between experiment, the corners only need to be identified once. From the ongoing example, **Figure 6** shows the estimated corners on the experimental brightfield image as red dots.

Now, with the estimated corners based on our robust feature matching, we enforce that the sensor array is a rectangle by obtaining another homography matrix and warping the experimental sensor array area onto it. **Figure 7** shows the final rectified image of the experimental sensor array. From our previous assumptions that the experimental setup does not move after the brightfield image is taken, these homography matrices can be used to trans-

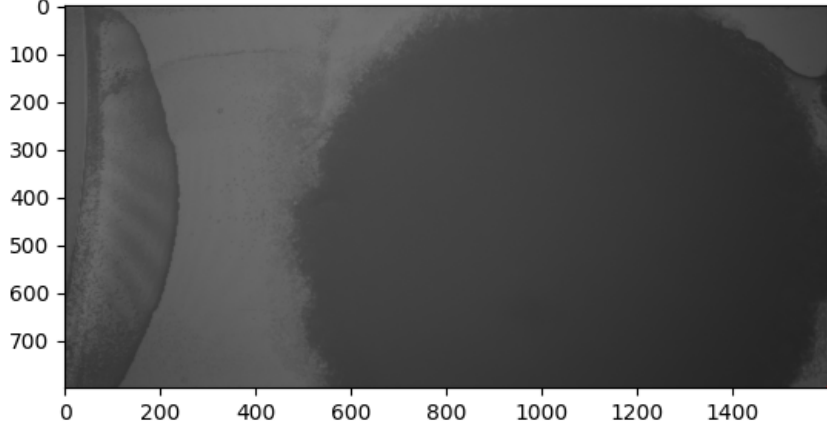


Figure 7: Rectified experimental brightfield image by transforming estimated corners into a rectangle.

form any experimental image taken during the length of the experiment.

Our algorithm to match the optical microscope fluorescence image to the impedance image is then described as follows: (1) Equalize contrast histograms between clean and experimental brightfield, (2) find SIFT interest points and keypoint descriptors [19], (3) perform nearest neighbor matching with Lowe ratio test [19], (4) perform RANSAC on the matches [10], (5) estimate corners of the sensor array based on transformation matrix and known corners on the clean image, and (6) rectify the estimated corners into a rectangle. Using this algorithm, we can obtain robustly matched sets of experimental fluorescence microscope images and impedance images, which can later be used for deep learning data sets. Links to the code are provided in the appendix of the thesis.

### 3.3 Impedance Super-Resolution

This section introduces work to improve the low spatial resolution of EIT images using novel super-resolution (SR) algorithms developed for impedance sensor arrays. As an example, we demonstrate the algorithm on impedance images taken of two types of algae: *Cosmarium* and *Pediastrum*. An improvement in resolution provides better overall results to any future algorithm that the images will pass through. SR techniques try to fill in details of low-resolution (LR) images to produce a high-resolution (HR) image. These techniques are typically divided according to their input: a single LR image or multiple LR images of the same scene with slight differences [7]. In the single image case, deep learning systems infer spatial knowledge based off of training on pairs of LR and HR images. With multiple images, there is no need to infer details as the different images typically provide the extra detail as long as there is some kind of subpixel motion. In order to use these images, the motion needs to be predicted in post-processing to undo the motion, which is nontrivial. After that, the images can be upsampled and stacked together to obtain the HR image. For example, multiple video frames can be aligned and computationally merged, taking advantage of the fact that camera movement produces spatial shifts in the scene relative to the image sensor, which can produce a composite image with higher resolution than individual frames [32]. In our application, we take advantage of the many mutual capacitance images the EIS sensor array can obtain to generate our collection of shifted images for super-resolution.

### 3.3.1 Imaging Unicellular Algae

Algae are microorganisms with a wide diversity of shapes and sizes, which makes them a good candidate for testing the proposed super-resolution algorithms [3]. Here we use a mix of *Cosmarium* and *Pediastrum* (Carolina Biological, NC, USA). These two different algae have an approximate cell size between  $10\mu m - 50\mu m$  diameter. *Cosmarium* has a bi-lobose shape, while *Pediastrum* is most frequently observed in small clusters of several dozen cells, as seen in **Figure 8a, 8d**. These two types of algae were mixed together and distributed on top of the sensor array. While it is easy to identify the *Pediastrum* from the *Cosmarium* in optical images (**Figures 8b and 8e**), the two are more difficult to differentiate in the impedance images (**Figures 8c and 8f**). Using super-resolution on the impedance images, the sensor should better resolve the subcellular features present in the two algae.

In **Figure 9**, we zoom in on one *Cosmarium* cell and one *Pediastrum* cell with the kernel size set to  $11 \times 11$ , producing 120 different mutual capacitance images. We do not include the original impedance image with no offset, since that image is not a mutual capacitance image. In these figures, the greater the offset kernel distance, the greater the distortion. For instance in **Figure 9a**, the image at offset  $(\delta_i, \delta_j) = (1, 1)$  has two distinct dots that indicate the two lobes, while the image at offset  $(\delta_i, \delta_j) = (2, 2)$  is clearly a similar image with two lobes, but stretched and distorted in the direction of its offset kernel. Each of these LR images provides different amounts of detail about the cell,

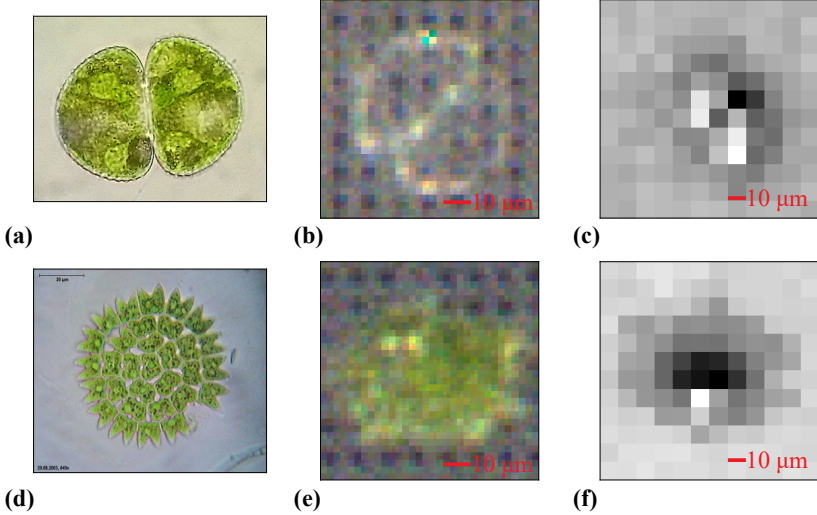
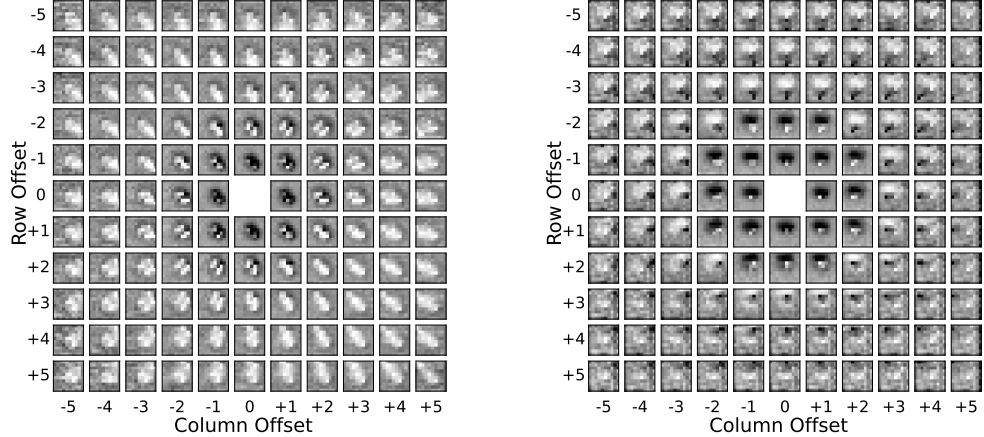


Figure 8: Images of two types of green algae. (a) A reference image of Cosmarium. (Atriplex82, CC BY-SA 4.0, via Wikimedia Commons.) (b) An optical microscope image of one cosmarium cell on the sensor array. (c) A single impedance image of the cosmarium cell from b. (d) A reference optical image of a cluster of pediastrum cells. (Dr. Ralf Wagner, CC BY-SA 3.0, via Wikimedia Commons) (e) An optical image of a cluster of pediastrum cells on the sensor array. (f) A single impedance image of the pediastrum cluster.

but contains a noticeable stretch and shift.

### 3.3.2 Shift-Sum Algorithm

Before introducing our algorithm for super-resolution on impedance sensor arrays, we acknowledge that similar work was done by Hu *et al.* with a smaller CMOS sensor array with the same capabilities for mutual impedance images [14]. In order to produce a composite SR image, their algorithm upsamples the original image with some interpolation (1), shifts the images by their offset kernel value (2), performs a shear mapping based on their offset kernel (3), and sums all the images together (4) [14]. While this algorithm produces composite



(a) Array of 120 mutual capacitance images of same Cosmarium algae with different offset kernels

(b) Array of 120 mutual capacitance images of same Pediastrum algae with different offset kernels.

Figure 9: A collection of 120 impedance images of one algae cell were acquired with offset kernels ( $\delta_i, \delta_j$ ) varied between  $-5 < \delta_i < +5$  and  $-5 < \delta_j < +5$ . While these are all images of the same cell, each offset kernel produces a different perspective. Note the spatial distortion of the algae based on the offset kernel.

images with better spatial resolution than their raw impedance counterpart, their stiff shear mapping can only correct for some directional skew, but not all possible linear distortion. In addition, performing shifts based off the actual offset value may cause misalignment and blurring.

### 3.3.3 Linear Deconvolution Algorithm

We produced a composite super-resolution impedance image using a procedure that involves (1) upsampling the original EIS images, (2) computing a linear filter to align each image to a common reference EIS image, (3) summing the realigned EIS images, and (4) applying a high-pass filter to compensate for in-

terpolation on the original low-resolution EIS images. To address all possible linear distortion and improve image alignment, we use linear deconvolution to approximate the filter that would undo the distortion in each image.

Recall that convolution operations performed in the spatial domain are equivalent to multiplication in the spatial frequency domain. Therefore, if we let  $a(x, y)$  and  $r(x, y)$  represent our input and output signals, respectively, and  $A(u, v)$  and  $R(u, v)$  represent their frequency domain representations, the linear filter,  $H$ , can be expressed as

$$H(u, v) = \frac{R(u, v)}{A(u, v)} \quad (1)$$

The common reference image is selected as one with a small offset vector (e.g.  $(+1, +1)$ ) that approximates the expected output signal with minimal spatial distortion. If  $a_i(x, y)$  represents our input upsampled high-passed image,  $r(x, y)$  represents our upsampled high-passed signal reference, and  $w(x, y)$  represents a zero-padded Hanning window to reduce spectral leakage, our algorithm for  $N$  images can be expressed as:

$$b(x, y) = \sum_{i=1}^N a_i(x, y) * \left( F^{-1} \left[ \frac{F(r(x, y))}{F(a_i(x, y))} \right] \cdot w(x, y) \right) \quad (2)$$

where  $b(x, y)$  is the computed SR-EIS image. The spatial alignment filter simultaneously solves for both lateral shifts and some types of image distortion, such as skew between different offset kernels.

In **Figure 10** and **Figure 11**, we apply this super-resolution algorithm to three instances of each of the two algae species, with  $N = 120$ . Although not all single raw images of *Cosmarium* reveal their two hemispheres, these were three examples where the bi-lobal structure was the most apparent in the raw images. Their respective SR-EIS images further enhance the bi-lobal structure while rounding the overall shape of the cell, consistent with microscopy images.

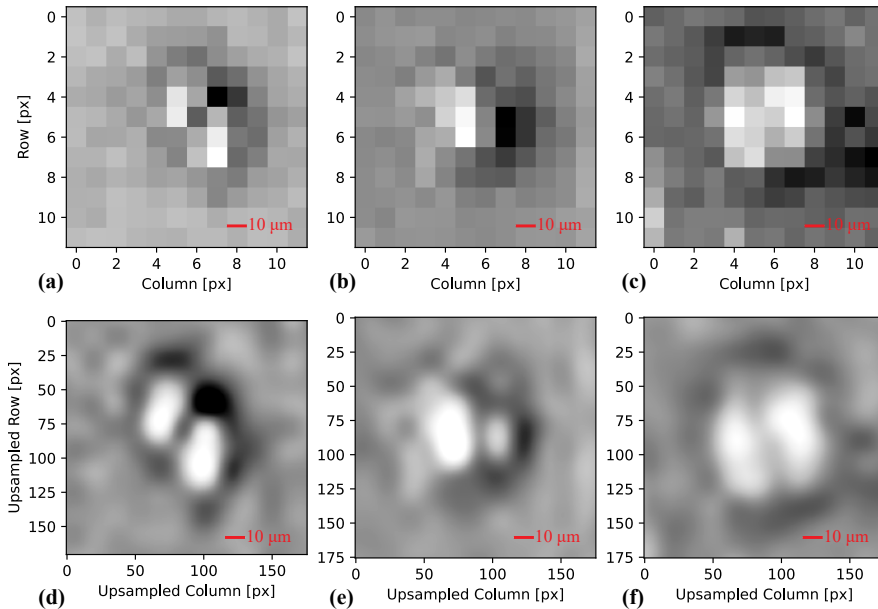


Figure 10: Super-resolution impedance (SR-EIS) reconstruction of three *Cosmarium* cells with their respective raw impedance reference. (a) Impedance image with offset kernel  $(\delta_i, \delta_j) = (-2, 0)$  (b) Impedance image with offset kernel  $(\delta_i, \delta_j) = (-2, -1)$  (c) Impedance image with offset kernel  $(\delta_i, \delta_j) = (-3, -1)$  (d, e, f) Linear deconvolution algorithm applied on 120 impedance images with reference image defined in (a,b,c).

For *Pediastrum*, single raw EIS images were unable to resolve individual cells within clusters. In the computed SR-EIS images, we were able to resolve more

detail in the shape of the cluster, with irregular boundary shapes, which likely correspond to ‘missing’ single cells from the edges of the cluster (similar to **Figure 8d**). We notice that cells may appear darker (lower impedance) for short offset vectors, but lighter (higher impedance) for larger offset vectors. This observation may relate to the cells’ 3-D shapes, as longer offset vectors have fringe fields that penetrate deeper into the sample [14]. This difference in polarity also leads to the dark outlines of the algae in the SR-EIS *Pediastrum* images. The composite images contain significantly more spatial information than the single *Pediastrum* images, although a precise physical interpretation of the spatial impedance profiles is complicated by the intensity and polarity changes with different offsets.

Investigating the SR-EIS image features further, we took linear slices through the composite and reference EIS images for *Cosmarium* and *Pediastrum* (Figure 12). The *Cosmarium* composite image slice shows improved resolution with a similar profile as the single-frame EIS image and confirms that the one-pixel features in the lower-resolution image are in fact the two hemispheres of the *Cosmarium*. For *Pediastrum*, the line profile once again highlights that the composite image includes finer spatial features within one cluster of cells. However, as mentioned previously, providing a physical explanation for the lower-impedance outline around the cell cluster remains an open challenge.

While these preliminary results are promising, we believe that further improvements could be achieved with improved reconstruction algorithms. For exam-

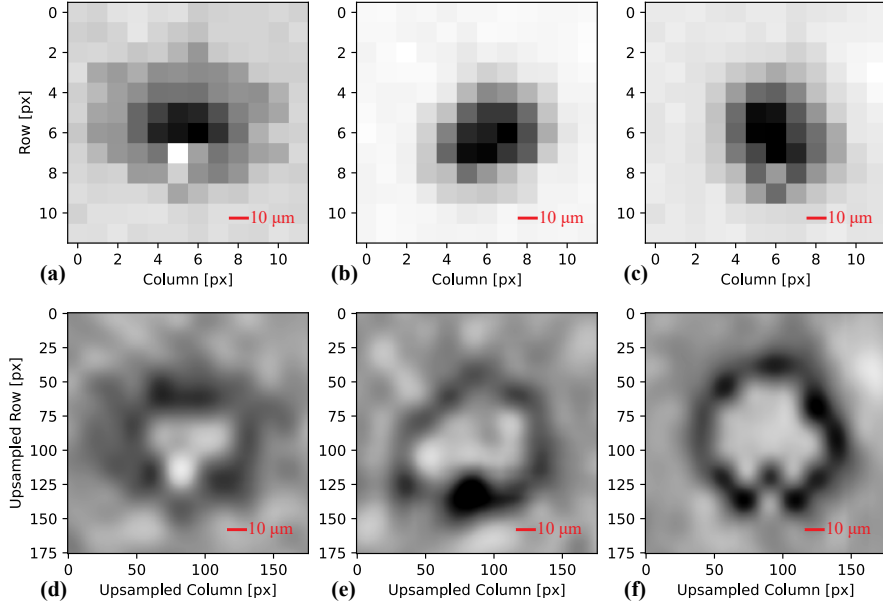


Figure 11: Super-resolution reconstruction of three pediastrum cells with their respective raw impedance reference. Offset kernel is chosen to show algae well in raw images. (a) Impedance image with offset kernel  $(\delta_i, \delta_j) = (+1, +1)$ . (b) Impedance image with offset kernel  $(\delta_i, \delta_j) = (+1, 0)$ . (c) Impedance image with offset kernel  $(\delta_i, \delta_j) = (0, +1)$ . (d, e, f) Linear deconvolution algorithm applied on 120 impedance images with reference image defined in (a,b,c).

ple, we should enforce radial symmetries based on offset kernels. Although it is also possible to add more offset kernel EIS images, mutual capacitance scales super-linearly [14], meaning that images further away may have a lower signal-to-noise ratio. It may also be worthwhile to pursue alternative super-resolution reconstruction techniques that could allow for nonlinear alignment filters, such as those built on deep learning models [31].

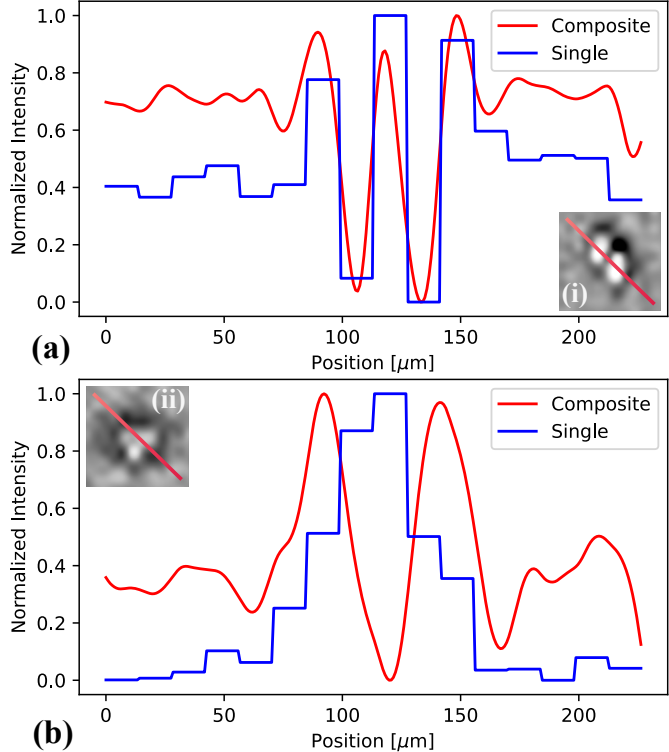


Figure 12: Algae line profile of a single EIS frame vs. composite SR-EIS. (a) Cosmarium slice taken across the isthmus to highlight its bi-lobal structure. The single EIS frame used has kernel offset  $(\delta_i, \delta_j) = (-2, 0)$ . (b) Pediastrum through same slice with single EIS frame with kernel offset  $(\delta_i, \delta_j) = (+1, +1)$ .

## 4 Computational Modeling of Bacterial Biofilms

Current biofilm models typically simulate the behavior of a single biofilm, its formation, and cell interactions [2] [13], but we are interested in the interactions between biofilms as they enable computation. There is one paper's model by Liu *et al.* that we originally replicate as it is the first to introduce the idea of inter-biofilm coupling and communication through electrical signalling [18]. This minimal mathematical model uses a modified Kuramoto

model where the coupling coefficient between different biofilms is dictated by nutrient concentration and cell phenotype. Nutrient concentration is itself a differential equation influenced by individual biofilm sizes and current phases. Perhaps the most important finding that this model produces is the synchronization of biofilm phases when nutrient concentration is high and anti-phase behavior to share nutrients when nutrient concentration is low. The specifics of the mathematical model in this paper are discussed in further detail in its supplementary material [18]. This paper models two biofilms, but our work extrapolates the model to large arrays of biofilms similar to other oscillator arrays seen in oscillator computing networks [6] [24].

## 4.1 Kuramoto Model

The Kuramoto model is a mathematical model typically used to describe the dynamics of a large system of similar coupled oscillators. It is especially prevalent in work modeling oscillating computers [8]. Since the Kuramoto model is the backbone of the biofilm model, we include the mathematical description here. Given  $N$  number of identical oscillators with some natural oscillation frequency,  $\omega_i$ , the Kuramoto model can be described as:

$$\frac{\theta_i}{dt} = \omega_i + \sum_{j=1}^N C_{ij} \cdot \sin(\theta_i - \theta_j), \quad (3)$$

where  $C_{ij}$  is the coupling coefficient between two oscillators [1]. Each oscillator has an independent natural frequency and phase, but the coupling coefficient term dictates how and when the system will synchronize. In the original biofilm

model, the coupling coefficient is dependent on the phenotype of the bacteria and the concentration of nutrients within the system [18]. The coupling coefficient is subject to change, which explains why higher initial concentrations of nutrients enable faster synchronization.

## 4.2 Extrapolated N biofilm Biofilm Model

To enable useful simulated computation on biofilms with our current knowledge, we developed an  $N$  biofilm model where the initial coupling coefficients are further defined with a weighted adjacency matrix, allowing the creation of graph-like structures. The code is available in the appendix. Adjacency matrices are  $N \times N$  symmetric matrices of booleans that describe the connections between  $N$  nodes in a graph. In each row  $i$ , the presence of 1 in each column  $j$ , indicates whether there is an edge between oscillator  $i$  and oscillator  $j$ . In **Figure 13**, we show an example of such an adjacency matrix. A weighted adjacency matrix allows for information beyond boolean values, enabling discussion of attributes such as distance between oscillators.

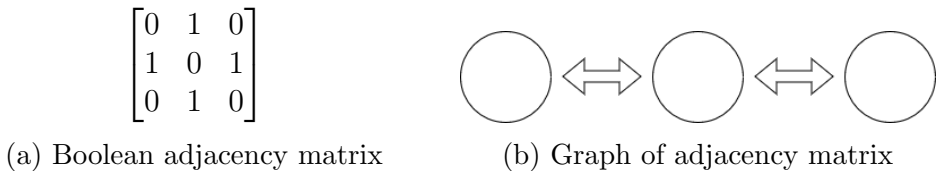


Figure 13: (a) An adjacency matrix of three nodes, where the middle node is connected to the end nodes. (b) The visual representation of the adjacency matrix.

Using the original biofilm paper model for two biofilms [18] and the Kuramoto

model for many coupled oscillators, we use our adjacency matrix to dictate the connections between biofilms. In addition, we add their consumption terms to the nutrient concentration equations and include an equation per biofilm to describe their size. This model was created in python using SciPy and NumPy and use the same parameters as the model created by Liu *et al.* [18]. Using Matplotlib, we also developed a visualization package for ensembles of three biofilms. In **Figure 14**, we show one frame of the visualization package running on the adjacency matrix noted in **Figure 13a**. Due to the low nutrient concentration in the system, the biofilm animation shows the biofilms 180 degrees out of phase with each other after convergence.

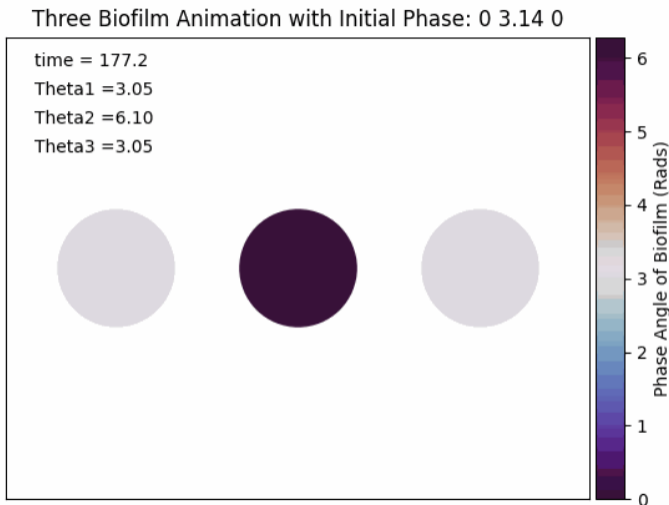


Figure 14: Capture of one frame of the visualization package. The three circles represents the biofilms and the color represents their phase. Due to the low nutrient concentration available, the biofilms are out of phase.

While we have yet to receive results experimentally on even the most simple extrapolation of the original coupled biofilm model, we are working with

biologists at Boston University to verify the model and provide insights into adjustments to the model. Alongside the super-resolution technologies proposed for EIS images, we hope to gain further understanding of inter-biofilm communication to tune these models.

## 4.3 Computer Microarchitectures of Biofilms

In this section, we introduce work that explores the space of possible architectures that biofilm oscillating arrays may occupy. We note that all of this work is done using the model introduced in the previous section, which does not capture the full picture of biofilm dynamics and requires experimental results to verify. We study Von-Neumann style computing by constructing a universal set of gates from the biofilms as well as more traditional problems that oscillator computer systems are proficient at.

### 4.3.1 Gate-Based Oscillator Computing

In gate-based boolean computing, the construction of a few specific gates allow for the creation of all possible boolean logic, known as functional completeness. This is known as universal sets of gates which include but are not limited to {NAND}, {NOR}, and {AND, OR, NOT}. In our biofilm system, the oscillators after convergence can be described as in-phase or out-of-phase with respect to some reference biofilm. We can use this phenomenon of in-phase and out-of-phase to represent 0 or 1, respectively. While it is certainly possible that biofilms may not be 180 degrees out of phase with each other, due to the large phase difference between distinct boolean states, that is not a problem.

One universal set that is particularly appealing to us is {MAJORITY, NOT} [20] because of the ease of construction of the majority gate in well-behaved oscillating systems. Imagine that we have three wires where each contain an

oscillating signal that is either in-phase or out-of-phase. If they are connected together and have one output wire, pairs of signals that are in-phase and out-of-phase will cancel each other out through destructive interference, leaving the signal in the majority. Similarly, when we have three signals in-phase with each other, their amplitude will increase. Since we are only concerned with the phase of the signal, the change in amplitude does not affect the computation. It has already been demonstrated that inverters can be created in nutrient sparse conditions, where biofilms go out of phase with each other [18].

By augmenting the initial phases of biofilms to establish inputs and using locally defined nutrient concentrations, it is possible to create each of the following gates in simulation. While not verified experimentally, it may be possible to use electrical signalling through electrode simulation to change initial phase based off of biological electrical signalling. Unfortunately, these systems are not viable because of the intrinsic memory biofilms hold and store. In addition, the time scale of electrical oscillations between biofilms is large enough that these systems could never compete with traditional semiconductor computing which uses the same method of computation. Therefore, while it is possible to create systems using traditional gate-based computing, we explore other options instead which can take advantage of the specific biofilm dynamics that we attributed to noise in this architecture.

## 5 Conclusions and Future Work

In this thesis, we discussed preliminary work done to further understanding of biofilm dynamics, mathematically model coupled biofilm arrays, and explore possible architectures to exploit computational behaviors of biofilms. We developed a robust image matching system between EIS images and microscope images that could be used to train GANs deep learning models, and a novel super-resolution algorithm using linear-deconvolution on mutual impedance images on EIS sensor arrays. Using these two methods, we hope to develop a end-to-end deep learning system in the near future where the input is a collection of mutual impedance images with different kernel offsets and the output is a high-resolution impedance image with fluorescence virtually applied. This technology will enable real-time monitoring of bacterial biofilms that was not previously possible due to phototoxicity. At the same time, we developed models of arrays of coupled biofilms based off of previous research. We hope to incorporate the findings of our continuous imaging system into the mathematical model. Lastly, we briefly explored gate-based oscillator architectures using our models. In the near future, we hope to experimentally verify small versions of our coupled biofilm model similar to the work achieved by Liu *et al.* [18].

We hope to explore the use of biofilms in traditional oscillator-based computing problems such as convolution, image processing, and optimization problems using our proposed models. [8]. Graph coloring is an NP hard optimization

problem where provided a mathematical graph, one needs to minimally color each node such that no two nodes which share an edge are the same color. It requires an exponential amount of traditional computing resources scaling against larger graphs [21], but research has shown that oscillator based computing systems can solve with near 100x speedups [21].

There is still a lot of work to be done to realize bacterial biofilms as viable computational devices. For instance, one of the perceived benefits to biologically-assisted computing is the potential energy savings due to the inherent optimization in biology, but we have yet to show this is the case. In addition, there is always work that can be done to understand the underlying mechanics of biofilms. Other roadblocks that need to be addressed include ease of manufacturing, robustness, and speed of the technology.

The methods proposed in this thesis on EIS sensor arrays is relevant beyond biofilms and can be used to image any kind microorganism. In addition, the work concerning modeling may be useful beyond computing applications, as biofilms represent a large issue in healthcare.

## Acknowledgements

I would like to thank Kangping Hu for his work interfacing with the EIS semiconductor systems, as well as his work taking images of algae for the super-resolution part of the thesis. In addition, I would like to thank Joey Incandela and Professor Joe Larkin at Boston University for their expertise in biofilm dynamics and biology along with their work to produce countless sets of biofilm EIS data for analysis.

## References

- [1] Juan Acebron et al. “The Kuramoto model: A simple paradigm for synchronization phenomena”. In: *Reviews of Modern Physics* 77 (Apr. 2005). DOI: [10.1103/RevModPhys.77.137](https://doi.org/10.1103/RevModPhys.77.137).
- [2] Rafael D. Acemel, Fernando Govantes, and Alejandro Cuetos. “Computer simulation study of early bacterial biofilm development”. en. In: *Scientific Reports* 8.1 (Mar. 2018). Number: 1 Publisher: Nature Publishing Group, p. 5340. ISSN: 2045-2322. DOI: [10.1038/s41598-018-23524-x](https://doi.org/10.1038/s41598-018-23524-x). URL: <https://www.nature.com/articles/s41598-018-23524-x> (visited on 04/11/2022).
- [3] Christopher E. Arcadia et al. “CMOS Electrochemical Imaging Arrays for the Detection and Classification of Microorganisms”. In: *2021 IEEE International Symposium on Circuits and Systems (ISCAS)*. ISSN: 2158-1525. May 2021, pp. 1–5. DOI: [10.1109/ISCAS51556.2021.9401471](https://doi.org/10.1109/ISCAS51556.2021.9401471).
- [4] Ricardo Augusto Borsoi et al. “Super-resolution reconstruction of electrical impedance tomography images”. en. In: *Computers & Electrical Engineering* 69 (July 2018), pp. 1–13. ISSN: 0045-7906. DOI: [10.1016/j.compeleceng.2018.05.013](https://doi.org/10.1016/j.compeleceng.2018.05.013). URL: <https://www.sciencedirect.com/science/article/pii/S0045790617333888> (visited on 04/05/2022).
- [5] Benoit Brazey, Yassine Haddab, and Nabil Zemiti. “Robust imaging using electrical impedance tomography: review of current tools”. In: *Proceedings of the Royal Society A: Mathematical, Physical and Engineering Sciences* 478.2258 (Feb. 2022). Publisher: Royal Society, p. 20210713.

- DOI: 10.1098/rspa.2021.0713. URL: <https://royalsocietypublishing.org/doi/10.1098/rspa.2021.0713> (visited on 04/05/2022).
- [6] Gyorgy Csaba and Wolfgang Porod. “Coupled oscillators for computing: A review and perspective”. In: *Applied Physics Reviews* 7.1 (Mar. 2020). Publisher: American Institute of Physics, p. 011302. DOI: 10.1063/1.5120412. URL: <https://aip.scitation.org/doi/10.1063/1.5120412> (visited on 04/02/2022).
  - [7] Lili Dong et al. “Selection-Based Subpixel-Shifted Images Super-Resolution”. In: *IEEE Access* 7 (2019). Conference Name: IEEE Access, pp. 110951–110963. ISSN: 2169-3536. DOI: 10.1109/ACCESS.2019.2934498.
  - [8] Yan Fang et al. “A Simplified Phase Model for Simulation of Oscillator-Based Computing Systems”. In: *ACM Journal on Emerging Technologies in Computing Systems* 13.2 (Dec. 2016), 14:1–14:20. ISSN: 1550-4832. DOI: 10.1145/2976743. URL: <https://doi.org/10.1145/2976743> (visited on 04/02/2022).
  - [9] Hooman Farkhani et al. “LAO-NCS: Laser Assisted Spin Torque Nano Oscillator-Based Neuromorphic Computing System”. In: *Frontiers in Neuroscience* 13 (2020). ISSN: 1662-453X. URL: <https://www.frontiersin.org/article/10.3389/fnins.2019.01429> (visited on 04/05/2022).
  - [10] Martin A. Fischler and Robert C. Bolles. “Random sample consensus: a paradigm for model fitting with applications to image analysis and automated cartography”. In: *Communications of the ACM* 24.6 (June 1981),

- pp. 381–395. ISSN: 0001-0782. DOI: 10.1145/358669.358692. URL: <https://doi.org/10.1145/358669.358692> (visited on 04/07/2022).
- [11] Udit Gupta et al. “Chasing Carbon: The Elusive Environmental Footprint of Computing”. In: *IEEE Micro* (2022). Conference Name: IEEE Micro, pp. 1–1. ISSN: 1937-4143. DOI: 10.1109/MM.2022.3163226.
- [12] R. A. Hoebe et al. “Controlled light-exposure microscopy reduces photobleaching and phototoxicity in fluorescence live-cell imaging”. en. In: *Nature Biotechnology* 25.2 (Feb. 2007). Number: 2 Publisher: Nature Publishing Group, pp. 249–253. ISSN: 1546-1696. DOI: 10.1038/nbt1278. URL: <https://www.nature.com/articles/nbt1278> (visited on 04/11/2022).
- [13] Harald Horn and Susanne Lackner. “Modeling of biofilm systems: a review”. eng. In: *Advances in Biochemical Engineering/Biotechnology* 146 (2014), pp. 53–76. ISSN: 0724-6145. DOI: 10.1007/10\_2014\_275.
- [14] Kangping Hu, Christopher E. Arcadia, and Jacob K. Rosenstein. “Super-Resolution Electrochemical Impedance Imaging with a  $100 \times 100$  CMOS Sensor Array”. In: *bioRxiv* (2021). DOI: 10.1101/2021.08.19.456729. eprint: <https://www.biorxiv.org/content/early/2021/08/19/2021.08.19.456729.full.pdf>. URL: <https://www.biorxiv.org/content/early/2021/08/19/2021.08.19.456729>.
- [15] Kangping Hu et al. “A  $13.1 \text{ mm}^2$   $512 \times 256$  Multimodal CMOS Array for Spatiochemical Imaging of Bacterial Biofilms”. In: *2022 IEEE Custom Integrated Circuits Conference (CICC) (in press)*. 2022.

- [16] S. Kalies, K. Kuettelmeyer, and A. Heisterkamp. “Mechanisms of high-order photobleaching and its relationship to intracellular ablation”. In: *Biomedical Optics Express* 2.4 (Mar. 2011), pp. 805–816. ISSN: 2156-7085. DOI: 10.1364/BOE.2.000816. URL: <https://www.ncbi.nlm.nih.gov/pmc/articles/PMC3072123/> (visited on 04/11/2022).
- [17] Maria Kostakioti, Maria Hadjifrangiskou, and Scott J. Hultgren. “Bacterial Biofilms: Development, Dispersal, and Therapeutic Strategies in the Dawn of the Postantibiotic Era”. In: *Cold Spring Harbor Perspectives in Medicine* 3.4 (Apr. 2013), a010306. ISSN: 2157-1422. DOI: 10.1101/cshperspect.a010306. URL: <https://www.ncbi.nlm.nih.gov/pmc/articles/PMC3683961/> (visited on 04/04/2022).
- [18] Jintao Liu et al. “Coupling between distant biofilms and emergence of nutrient time-sharing”. In: *Science* 356.6338 (2017), pp. 638–642. DOI: 10.1126/science.aah4204. eprint: <https://www.science.org/doi/pdf/10.1126/science.aah4204>. URL: <https://www.science.org/doi/abs/10.1126/science.aah4204>.
- [19] David G. Lowe. “Distinctive Image Features from Scale-Invariant Keypoints”. In: *Int. J. Comput. Vision* 60.2 (Nov. 2004), pp. 91–110. ISSN: 0920-5691. DOI: 10.1023/B:VISI.0000029664.99615.94. URL: <http://dx.doi.org/10.1023/B:VISI.0000029664.99615.94>.
- [20] Abdulqader Mahmoud et al. “Fan-out enabled spin wave majority gate”. In: *AIP Advances* 10.3 (Mar. 2020). Publisher: American Institute of

- Physics, p. 035119. DOI: 10.1063/1.5134690. URL: <https://aip.scitation.org/doi/10.1063/1.5134690> (visited on 04/11/2022).
- [21] Antik Mallick et al. “Graph Coloring Using Coupled Oscillator-Based Dynamical Systems”. In: *2021 IEEE International Symposium on Circuits and Systems (ISCAS)*. ISSN: 2158-1525. May 2021, pp. 1–5. DOI: 10.1109/ISCAS51556.2021.9401188.
- [22] Igor L. Markov. “Limits on fundamental limits to computation”. en. In: *Nature* 512.7513 (Aug. 2014). Number: 7513 Publisher: Nature Publishing Group, pp. 147–154. ISSN: 1476-4687. DOI: 10.1038/nature13570. URL: <https://www.nature.com/articles/nature13570> (visited on 04/02/2022).
- [23] OpenCV. *Open Source Computer Vision Library*. 2015.
- [24] Juan Manuel Parrilla-Gutierrez et al. “A programmable chemical computer with memory and pattern recognition”. en. In: *Nature Communications* 11.1 (Mar. 2020). Number: 1 Publisher: Nature Publishing Group, p. 1442. ISSN: 2041-1723. DOI: 10.1038/s41467-020-15190-3. URL: <https://www.nature.com/articles/s41467-020-15190-3> (visited on 04/02/2022).
- [25] Xiang Ren et al. “Cardiac Muscle Cell-Based Coupled Oscillator Network for Collective Computing”. en. In: *Advanced Intelligent Systems* 3.4 (2021). \_eprint: <https://onlinelibrary.wiley.com/doi/pdf/10.1002/aisy.202000253>, p. 2000253. ISSN: 2640-4567. DOI: 10.1002/aisy.202000253. URL:

- <https://onlinelibrary.wiley.com/doi/abs/10.1002/aisy.202000253> (visited on 04/02/2022).
- [26] Yair Rivenson et al. “Virtual histological staining of unlabelled tissue-autofluorescence images via deep learning”. en. In: *Nature Biomedical Engineering* 3.6 (June 2019). Number: 6 Publisher: Nature Publishing Group, pp. 466–477. ISSN: 2157-846X. DOI: 10.1038/s41551-019-0362-y. URL: <https://www.nature.com/articles/s41551-019-0362-y> (visited on 04/05/2022).
- [27] Divakar Sharma, Lama Misba, and Asad U. Khan. “Antibiotics versus biofilm: an emerging battleground in microbial communities”. In: *Antimicrobial Resistance & Infection Control* 8.1 (May 2019), p. 76. ISSN: 2047-2994. DOI: 10.1186/s13756-019-0533-3. URL: <https://doi.org/10.1186/s13756-019-0533-3> (visited on 04/04/2022).
- [28] L Song et al. “Photobleaching kinetics of fluorescein in quantitative fluorescence microscopy.” In: *Biophysical Journal* 68.6 (June 1995), pp. 2588–2600. ISSN: 0006-3495. URL: <https://www.ncbi.nlm.nih.gov/pmc/articles/PMC1282169/> (visited on 04/11/2022).
- [29] Damir Vodenicarevic et al. “A Nanotechnology-Ready Computing Scheme based on a Weakly Coupled Oscillator Network”. en. In: *Scientific Reports* 7.1 (Mar. 2017). Number: 1 Publisher: Nature Publishing Group, p. 44772. ISSN: 2045-2322. DOI: 10.1038/srep44772. URL: <https://www.nature.com/articles/srep44772> (visited on 04/05/2022).

- [30] M. Mitchell Waldrop. “More than Moore”. English. In: *Nature* 530.7589 (Feb. 2016). Publisher: Nature Publishing Group, pp. 144–148. ISSN: 00280836. URL: <https://go.gale.com/ps/i.do?p=HRCA&sw=w&issn=00280836&v=2.1&it=r&id=GALE%7CA443132364&sid=googleScholar&linkaccess=abs> (visited on 04/02/2022).
- [31] Zhihao Wang, Jian Chen, and Steven C. H. Hoi. “Deep Learning for Image Super-resolution: A Survey”. In: *arXiv:1902.06068 [cs]* (Feb. 2020). arXiv: 1902.06068. URL: <http://arxiv.org/abs/1902.06068> (visited on 04/09/2022).
- [32] Bartłomiej Wronski et al. “Handheld Multi-Frame Super-Resolution”. In: *ACM Transactions on Graphics* 38.4 (Aug. 2019). arXiv: 1905.03277, pp. 1–18. ISSN: 0730-0301, 1557-7368. DOI: [10.1145/3306346.3323024](https://doi.org/10.1145/3306346.3323024). URL: <http://arxiv.org/abs/1905.03277> (visited on 04/09/2022).
- [33] Chih-Yu Yang et al. “Encoding Membrane-Potential-Based Memory within a Microbial Community”. eng. In: *Cell Systems* 10.5 (May 2020), 417–423.e3. ISSN: 2405-4720. DOI: [10.1016/j.cels.2020.04.002](https://doi.org/10.1016/j.cels.2020.04.002).

## 6 Appendix

Links to Code: At the moment, github repos exist for all of the code, but we have yet to make any of it public.